Supporting Information

Photoluminescence Mapping of Mobile and Fixed Defects in Halide Perovskite Films

Sarah C. Gillespie,[†,‡] Jérôme Gautier,[†] Linde M. van de Ven,[†] Agustin O. Alvarez,[†] Bruno Ehrler,[†] L.J. Geerligs,[‡] Veronique S. Gevaerts,[‡] Gianluca Coletti,[¶] and Erik C. Garnett[*,†,§]

†*LMPV-Sustainable Energy Materials Department, AMOLF Institute, Science Park 104, Amsterdam, 1098XG, The Netherlands*

‡*TNO Department Solar Energy, Westerduinweg 3, Petten, 1755LE, The Netherlands*

¶*School of Photovoltaic and Renewable Energy Engineering, University of New South Wales, Sydney, New South Wales 2052, Australia*

§*University of Amsterdam, Science Park 904, Amsterdam, 1098XH, The Netherlands*

E-mail: e.garnett@amolf.nl

Contents

S1 Sample Fabrication

In a nitrogen-filled glovebox, two 1.5 M solutions of PbI_2 (≥99.99%, TCI) and $PbBr_2$ (≥98%, TCI) were prepared in DMF:DMSO (4:1 by volume) and stirred overnight at 70 °C. The PbI_2 solution was combined with FAI powder (≥99%, TCI) and excess DMF:DMSO solvent to yield a 1.24 M $FAPbI_3$ solution containing 10 mol% excess PbI_2. Similarly, the $PbBr_2$ solution was combined with MABr (≥99%, TCI) to form a 1.24 M $MAPbBr_3$ solution, also with a 10 mol% $PbBr_2$ excess. Both perovskite solutions were stirred for an additional 2 hours at 70 °C. The solutions were then mixed in an 80:20 ratio ($FAPbI_3$:$MAPbBr_3$), followed by the addition of a 1.5 M CsI solution in DMSO (≥99.99%, Sigma-Aldrich) to achieve the final composition $Cs_{0.07}(FA_{0.8}MA_{0.2})_{0.93}Pb(I_{0.8}Br_{0.2})_3$. The resulting solution was stirred at 70 °C for another 2 hours before cooling to room temperature and filtering through a 0.45 µm PTFE filter.

Glass substrates were cleaned by scrubbing them with a 1% Hellmanex III solution in deionized (DI) water, followed by applying sequential sonication steps (15 minutes each) in 70 °C water, acetone, and finally in isopropanol. Immediately before perovskite spin-coating, the substrates were treated under UV-ozone for 30 minutes and then transferred into the glovebox.

120 µL of the precursor solution was dispensed onto the glass substrate and subsequently spin-coated at 5000 RPM for 30 seconds after a 6 second ramp-up time. At 15 seconds before the end of the cycle, 170 µL of chlorobenzene filtered through a 0.22 µm PTFE filter was deposited as an antisolvent. The films were annealed on a hotplate at 100 °C for 45 minutes. Finally, the films were encapsulated with 60 nm of SiO_2, deposited by electron-beam evaporation (Polyteknik Flextura M508E), directly from a SiO_2 target at a deposition rate of 0.06 nm/s. We use SiO_2 as we have previously shown that electron-beam evaporated SiO_2 functions well as an inert, stabilizing and passivating layer[1,2].

S2 Time-Resolved Photoluminescence Spectroscopy

The time-resolved photoluminescence decay trace for the thin film was obtained with a time-correlated single-photon counting (TCSPC) system (PicoQuant), comprised of a PDL 828 Sepia II, a HydraHarp, a 485 nm pulsed diode laser and an Olympus ×60 Plan Apochromat water objective. The TRPL decay was measured following approximately 2 minutes of continuous light soaking. The total decay was averaged across an 80 µm×80 µm map with a 400 nm step size between each pixel. The laser repetition rate was set to 1 MHz, sufficiently low to capture the entire PL decay[3]. An arbitrary fit was applied to the TRPL signal to reduce noise, before the fit was background corrected by subtracting the noise floor from the signal. This decay is shown in Figure S1a. From measuring the film thickness by profilometry, absorptance, laser fluence (0.136 mJ/cm^2) and the laser spot size (1/e^2 diameter = 2 µm), the excess minority carrier density generated from each pulse was determined, $\Delta n_0 = 4.248\times10^{18}$ cm^{-3}. From this starting carrier density, the complete PL decay trace was converted to the decay of excess carrier density using $\Delta n \propto \sqrt{\mathrm{PL}}$. Then, the differential lifetime was calculated as a function of Δn with the differential lifetime equation:

$$\tau_{\mathrm{diff}}(\Delta n) = -\left(\frac{\mathrm{d}\ln\Delta n(t)}{\mathrm{d}t}\right)^{-1} \tag{S1}$$

By definition, the saturation point of this curve is where $\tau_{\mathrm{diff}} = \tau_{\mathrm{trap}} = 100.5$ ns (Figure S1b)[4].

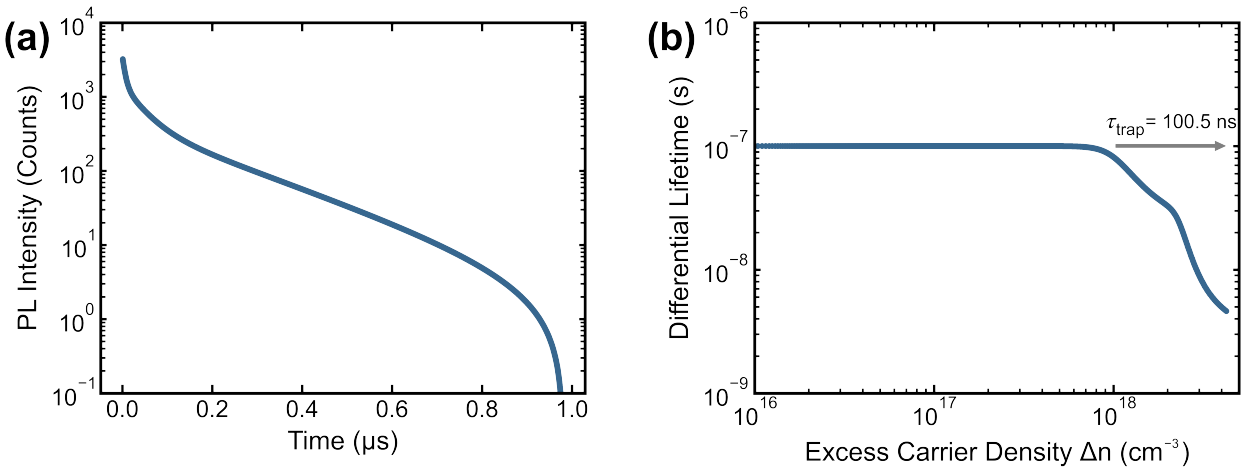

Figure S1: (a) Arbitrary fit of the averaged raw PL decay trace of the encapsulated perovskite thin film sample, following noise floor signal subtraction. (b) Differential lifetime as a function of excess minority carrier density, Δn. The saturation point is indicated with the gray arrow, in which $\tau_{diff} = \tau_{trap} = 100.5$ ns[4].

S3 Photoluminescence Quantum Yield

Photoluminescence quantum yield maps were collected using a custom-built integrating sphere microscopy setup and software; a schematic is shown in our previous work[5]. 660 nm excitation was provided using a 78 MHz supercontinuum laser (NKT Fianium FIU 15) coupled to an acousto-optical tunable filter (AOTF, with a Gooch & Housego AODS20200-8 driver). The AOTF was programmed to select the appropriate excitation wavelength, intensity and to modulate the laser light based on the input reference frequency. The beam radius was measured to be 800 nm using the knife-edge technique. Two PDA100A Si photodetectors were used as a beam monitor (BM) detector and as a reflection (R) detector. The BM detector collected the light emitted directly from the laser. The R detector collected light that was directly reflected or emitted within the acceptance angle of the objective lens from the integrating sphere after sample interaction. A calibrated Newport 818-UV photodetector was used to collect the transmitted and scattered light from the integrating sphere (IS), and to convert the signal intensity to photon counts. All detectors were connected to three lock-in amplifiers (LIA, Stanford Research Systems SR830). One LIA was used to set the

reference frequency, which was transmitted to the AOTF and to the other LIAs. The reference frequency was set to 1.253 kHz. Four reference measurements were performed: a blank to calibrate the PDA100A detectors, a filter leakage reference, a 100% transmission reference, and a 100% reflection reference. The reflection reference was measured with a silver-coated mirror placed at the same position as the sample during the PLQY measurement (ThorLabs PF10-03-P01). 700 nm short-pass and long-pass filters (placed in front of the reflection and IS detectors) were used to separate the absorptance and PL data, respectively. In addition to selecting the laser intensity using the AOTF, ND filters were applied to sweep the intensity range. The sample was mounted on an external piezo stage while in the integrating sphere, which enabled spatial maps to be obtained. For every measurement, the emission data was obtained first, then the absorptance (A) data was collected. After calibration to convert the raw detector signals to number of photons (Φ) and accounting for the reference measurements, the PLQY was determined using the standard:

$$\text{PLQY} = \frac{\Phi_{PL}}{\Phi_{\text{abs}}} = \frac{\Phi_{PL,R} + \Phi_{PL,IS}}{\Phi_{\text{exc}} \times A} \tag{S2}$$

where $\Phi_{PL,R}$ and $\Phi_{PL,IS}$ represent the number of emitted photons incident on the R detector and the IS detector. The IS detector was used to collect both transmission, T, and scattering, S. With the short-pass filters before the detectors, the absorptance was calculated using $A = 1 - R - S - T$. For the PLQY data collected for Figure S12 later presented in Section S5, 5 µm×5 µm PLQY maps were collected at each intensity. From these maps, the average PLQY and associated uncertainty at each intensity point was determined. Exemplary maps of the absorptance and PLQY are shown in Figure S2.

In the case of Figure 1 in the main text, the PLQY time series was obtained by flipping between the short-pass and long-pass filters during the measurement window. To assess reproducibility, time series measurements were repeated nine times for a perovskite sample identical in composition and fabrication methods to that shown in Figure 1. The repeated

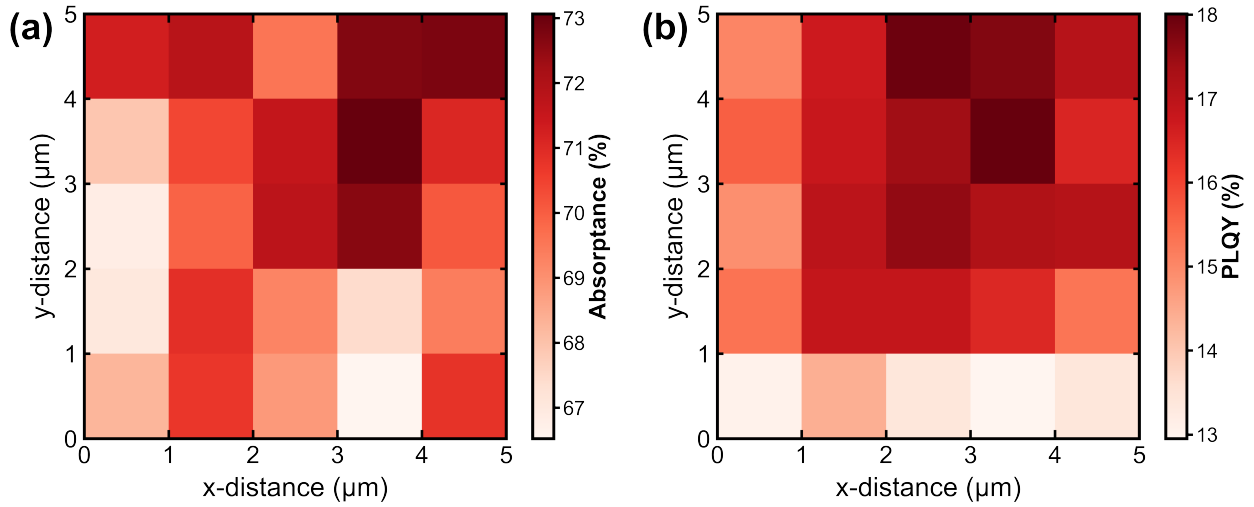

Figure S2: (a) Absorptance map of the perovskite thin film measured under an incident photon flux of $\Phi_{\text{exc}} = 5.88 \times 10^{20}$ cm^{-2}/s. Within this map, the average absorptance and standard deviation are $A = 70.1\%$ and $\sigma_A = 1.9\%$. (b) Corresponding PLQY map for the same area. The average PLQY and standard deviation within the map are PLQY= 16.0% and $\sigma_{\text{PLQY}} = 1.6\%$.

measurements were collected on different points on the sample and are presented in Figure S3. The mean PLQY over time is shown with the black dashed curve and the standard deviation (σ) is shown in gray. Given the similarities across all repeated measurements, we confirm that the general bi-exponential rise trends are reproducible across different sample spots.

In the main text, the reproducible bi-exponential rise of the PLQY, as shown in Figure 1 and in Figure S3, is attributed to a reduction in the trap-state density (thus a reduction in the trap-assisted recombination rate) over time. Other mechanisms such as surface reactions or passivating atmospheric reactions were ruled out as we have shown in our previous works that the SiO_2 encapsulation reduces sample reactivity with the atmosphere and prevents sample degradation[1,2,6,7]. Thermal relaxation processes were also considered and subsequently ruled out; in a purely thermal diffusion model for our sample, the glass substrate is the limiting layer. The thickness of the substrate was measured as $L_{\text{glass}} = 1$ mm, and the literature value for the thermal diffusivity of glass was taken as $\alpha \approx 8{\times}10^{-3}$ cm^2/s[8]. From this, the thermal relaxation time constant $\tau_{\text{therm}} = L^2_{\text{glass}}/\alpha_{\text{glass}}$ is on the order of 1 second. This is much faster

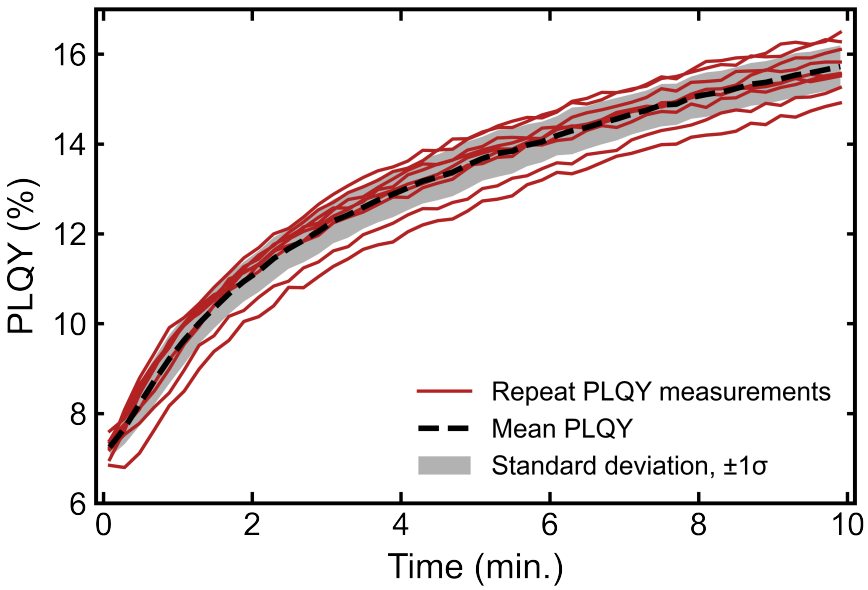

Figure S3: Repeated PLQY time series measurements (red) over a 10 minute measurement window for nine different spots on the sample. The average PLQY is shown with the black, dashed curve, while the standard deviation is shown in gray. Within the 10 minute measurement window, the time-averaged mean PLQY is 12.99% and the time-averaged standard deviation is $\sigma_{\text{average}} = 0.47\%$.

than the observed changes over tens of minutes and thus cannot account for the extended PLQY trends.

S4 Intensity-Modulated Photoluminescence Spectroscopy

S4.1 Experimental Methods for IMPLS

The IMPLS setup shown in Figure 2a of the main text is comprised of a WITec alpha300 SR confocal imaging microscope, coupled to a S1DC405 405 nm CW diode laser (ThorLabs) and to a 450 nm light-emitting diode (Cree LED). The LED intensity and sinusoidal modulation was driven with a 33522A arbitrary waveform generator (Keysight Technologies). The 405 nm focused beam size was measured using the knife-edge technique and the power density and equivalent photon flux were determined with a wavelength-calibrated power meter (S120VC coupled to a PM100D, ThorLabs)[9].

As noted in the main text, the data collected corresponding to the results in Figure 3 was obtained under a collection randomizing protocol. In detail, this protocol included that each measurement was collected on a new, randomly assigned point on the sample located at least 50 µm from the previous point. The frequency and DC intensity sweeps were also collected in a random order to prevent any hysteresis effects (if present) from accumulating. Every measurement was collected approximately 3 - 4 minutes following the previous measurement. Finally, the PL data was only fit to a sinusoidal function after the DC PL signal stabilized, ensuring that thermal relaxation and other transient features were eliminated from this measurement.

All measurements were performed on encapsulated films since SiO_2 minimizes atmospheric reactions, enhances surface passivation and suppresses perovskite degradation under high-intensity excitation[1,2]. We note that repeating the experiments without encapsulation may introduce additional (transverse and lateral) migration pathways, such as iodine formation and subsequent evaporation from the film surface[10].

All IMPLS maps (Figure 4 and Figure S8) and all measurements relating to the uncertainty statistics (Figure S10 and Figure S11) were obtained using a home-built pulsed laser microscopy setup. A tunable laser (Chameleon Discovery NX, Coherent) set to 405 nm was coupled to a pulse picker (pulseSelect, APE) to produce pulses (80 fs pulse width) at a repetition rate of 4 MHz. The beam was spatially filtered and then focused onto the sample using a Mitutoyo M Plan APO NIR B ×50 objective. The size of the beam on the sample was adjusted by changing the focal length of the collimating lens after the spatial filter, and the spot size was calibrated using the knife-edge technique. The sample was mounted on a TRITOR 100 SG piezo stage (Piezosystem Jena), and the same 450 nm LED as above provided sinusoidal AC illumination from the rear of the perovskite sample. To collect the maps, the measurement sequence was randomized, with each consecutive point separated by at least 5 µm from the previous measurement. The total PL signal was collected using a Kymera 193i (Andor) and a ProEM electron-multiplying CCD (Princeton Instruments).

To determine Δn, the incident photon flux Φ was converted to the carrier generation rate G using $G = A\Phi/W_{\mathrm{pvk}}$, where the absorptance was $A = 72 \pm 2\%$ (measured as described in Section S3), and the film thickness $W_{\mathrm{pvk}} = 560$ nm (measured with profilometry). The excess carrier density was then obtained as $\Delta n = G\tau_{\mathrm{trap}}(\Delta n)$, assuming rapid spatial homogenization of the photogenerated excess carriers. This assumption is justified by the relatively high electronic mobilities ($\gtrsim 1$ cm^{2}V^{-1}s^{-1}) and long carrier lifetimes ($\gtrsim 100$ ns) for perovskite films[4,11,12]. The trap-assisted lifetime, $\tau_{\mathrm{trap}} = 100.5$ ns, was measured through TRPL spectroscopy as previously described in Section S2[1,4].

To maximize the signal-to-noise ratio across IMPLS measurements with different frequencies, different integration times were applied to acquire the spectra. To account for the differences in the integration times, the PL DC offset was scaled relative to the LED offset in each spectrum, as the absolute LED offset was constant for all measurements. Thus:

$$PL(f)_{\mathrm{DC,relative}} = \frac{PL(f)_{\mathrm{DC,counts}}}{LED(f)_{\mathrm{DC,counts}}} \tag{S3}$$

Where counts represent the integrated CCD counts for each spectrum. The PL amplitude was defined as the ratio between the PL peak value and the PL offset. Typically for other modulated techniques at high frequencies, the response amplitude is also scaled by the amplitude of the input parameter to correct for any frequency-dependent system response. However, given the low modulation frequency range explored in this work, the LED amplitude did not vary as a function of frequency (Figure S4) and so the PL amplitude did not need to be corrected further. Moreover, for every frequency point, the DC PL data remained constant across the measurement. This ensured that the observed changes in the PL offset signal in Figure 3c are due to probed ionic processes, and not from any external factor such as heating, degradation, or other frequency-independent chemical reactions.

S4.2 Supporting IMPLS Results

In this section, we present the additional relevant IMPLS experiments. In Figure S4, we compare the PL amplitude against the reference LED measurement. Over the relevant frequency window, we determined that changes in the observed amplitude were not due to modulation effects from the LED or other system effects. Figure S5 shows the evolution of the PL phase shift and PL amplitude as a function of Δn, with the different curves corresponding to different modulation frequencies f. Higher modulation frequencies slightly shift the onset of the phase shift toward larger Δn values (Figure S5a), while the PL amplitude at high Δn decreases with increasing modulation frequency (Figure S5b).

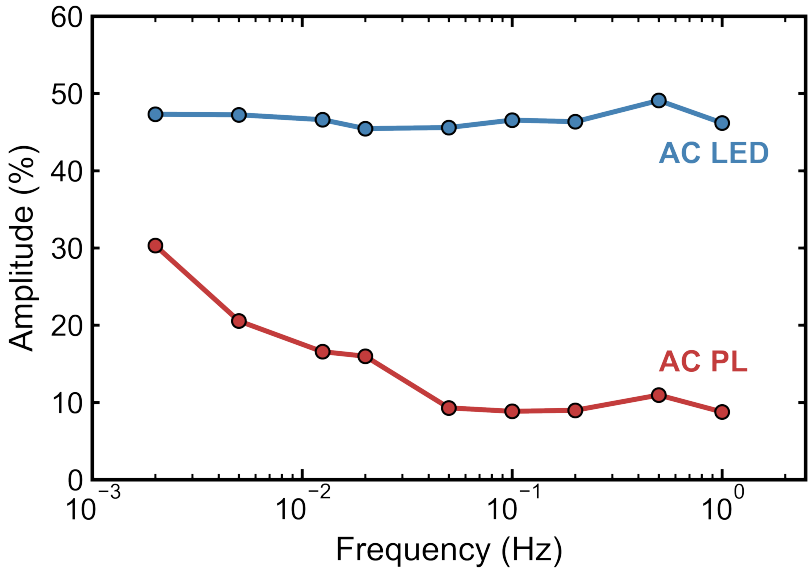

Figure S4: Comparison between the LED amplitude (blue) and the PL amplitude (red) as a function of frequency. The LED amplitude is independent of frequency, signifying that the change in the PL amplitude is due to the sample-related processes.

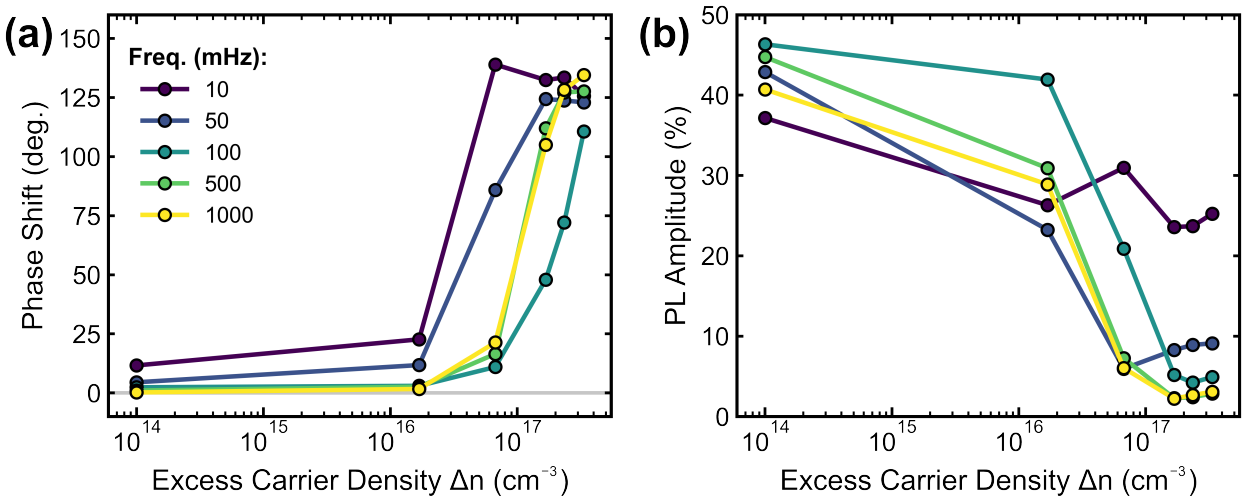

Figure S5: Line scans of the (a) PL phase shift and (b) PL amplitude as functions of Δn. Each color represents a different frequency applied during the measurement, labeled in the top left corner in panel (a).

In our previous IMPLS study, we attributed an observed slow process ($\tau_{\text{char,slow}} \approx 77$ s) to iodide vacancy diffusion across the depth of the sample. In the present work, we propose that a similar diffusive process involving mobile ions is being observed. However, in contrast to our earlier results – where the PL amplitude decreased with decreasing modulation frequency – we now observe an enhancement of the PL amplitude at low frequencies[13]. To determine whether this discrepancy arises from different excitation conditions, we repeated the frequency-dependent measurements without laser excitation and reduced the LED amplitude to 20% of its offset value. The results (Figure S6) show that under these conditions, IMPLS trends are consistent with our previous findings.

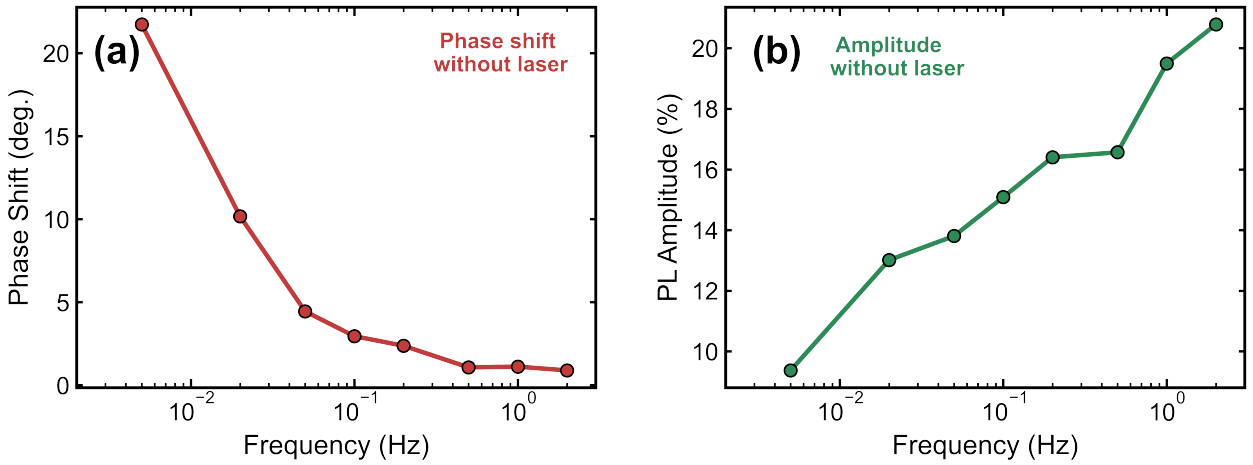

Figure S6: (a) PL phase shift and (b) PL amplitude as functions of modulating frequency without the additional laser excitation. For this measurement, the LED amplitude was reduced to 20% of its offset value. The sample's amplitude is reduced as frequency is reduced and the extent of the phase shift is significantly reduced without the additional laser excitation, compared to Figure 3. These trends in panels (a) and (b) agree with those observed for a similar perovskite composition in our previous work[13].

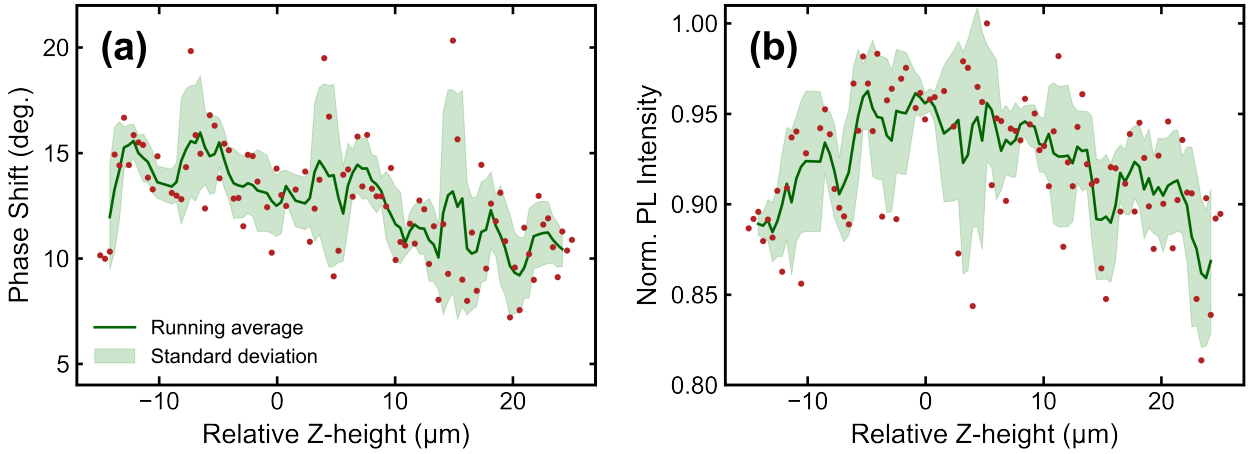

Figure S7: (a) PL phase shift and (b) PL intensity as a function of Z-height relative to the focal plane (Z-height = 0 μm). Experimental values are shown by the red markers, with the running average and standard deviation shown by the green solid lines and shaded regions, respectively.

In our earlier work, we attributed the decreasing PL amplitude to transverse (vertical) ionic diffusion toward the interface, leading to defect formation at the interface, thereby quenching the PL amplitude at low frequencies[13]. To further assess whether the IMPLS phase shift observed here instead originates from lateral ionic diffusion, we measured the phase shift and PL intensity as a function of Z-height relative to the focal plane (Figure S7, where the focal plane corresponds to Z-height = 0 µm). The phase shift remains reasonably independent of Z-height, compared to the expected PL intensity peak at Z = 0 µm. This indicates that the IMPLS response in this case is unlikely to be dominated by transverse ionic diffusion or associated surface reactions.

S4.3 PL Intensity and Phase Shift Spatial Maps

Using the custom-built pulsed laser setup, we constructed maps of the PL phase shift and PL intensity across 625 m^2 areas. The raw maps (before bicubic smoothing) corresponding to those shown in Figure 4 are presented in Figure S8, below. In addition, we measured the phase shift and PL intensity over the same area (and different than either areas in Figure S8) for three different frequencies $f = 500, 100, 50$ mHz. These were collected in a random order with several hours between each measurement to effectively reset the perovskite. The results (Figure S9) highlight that both the phase shift and PL intensity generally increased over the whole map as frequency was reduced, agreeing with the general trends presented in Figures 3a and 3c.

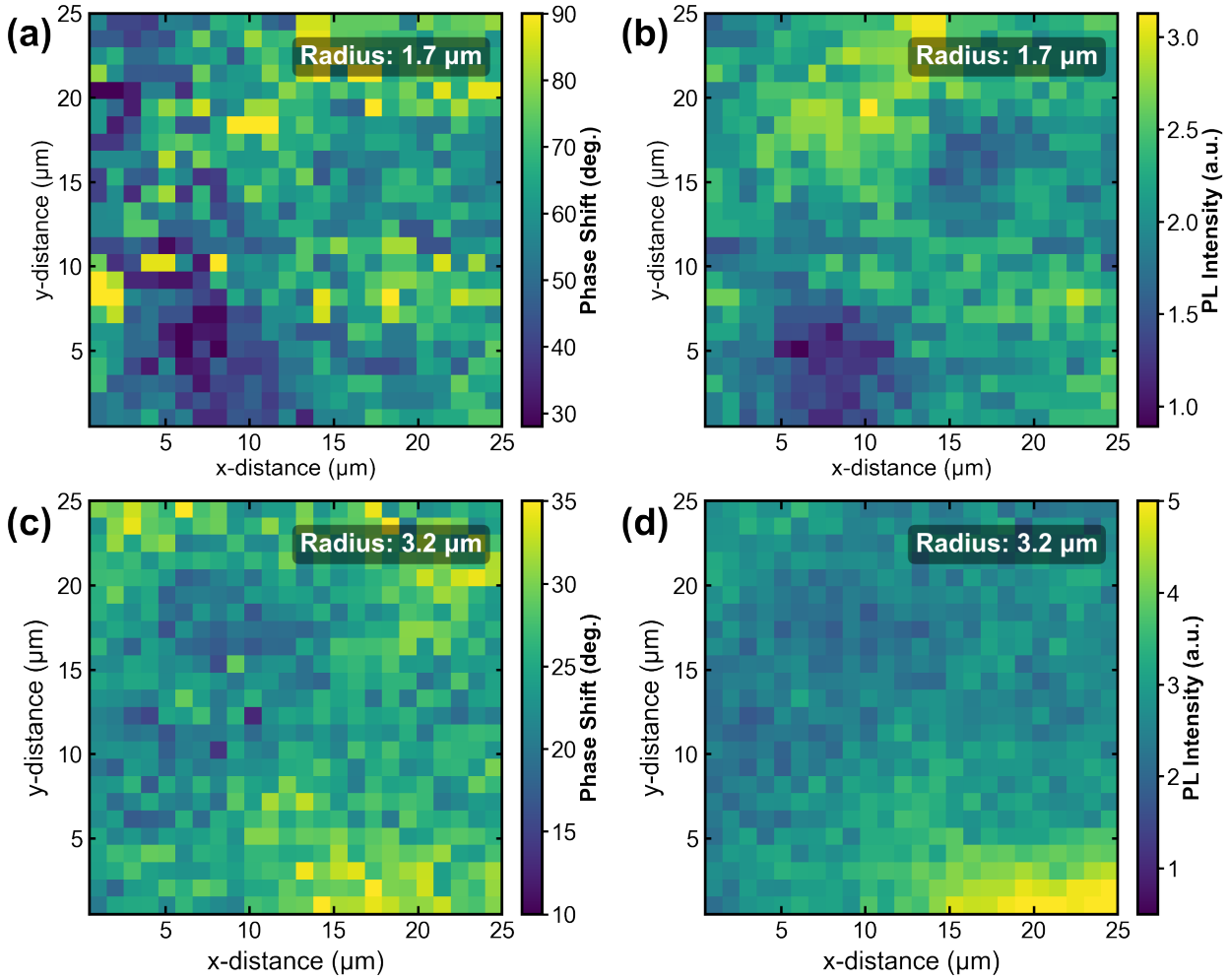

Figure S8: (a) Phase shift and (b) PL intensity raw signal maps (before bicubic smoothing) for a beam radius of 1.7 µm. (c) Phase shift and (d) PL intensity raw signal maps for a beam radius of 3.2 µm. The 3.2 µm measurement was performed on a different area of the same sample, at matched fluence and with the same modulation frequency (f = 50 mHz).

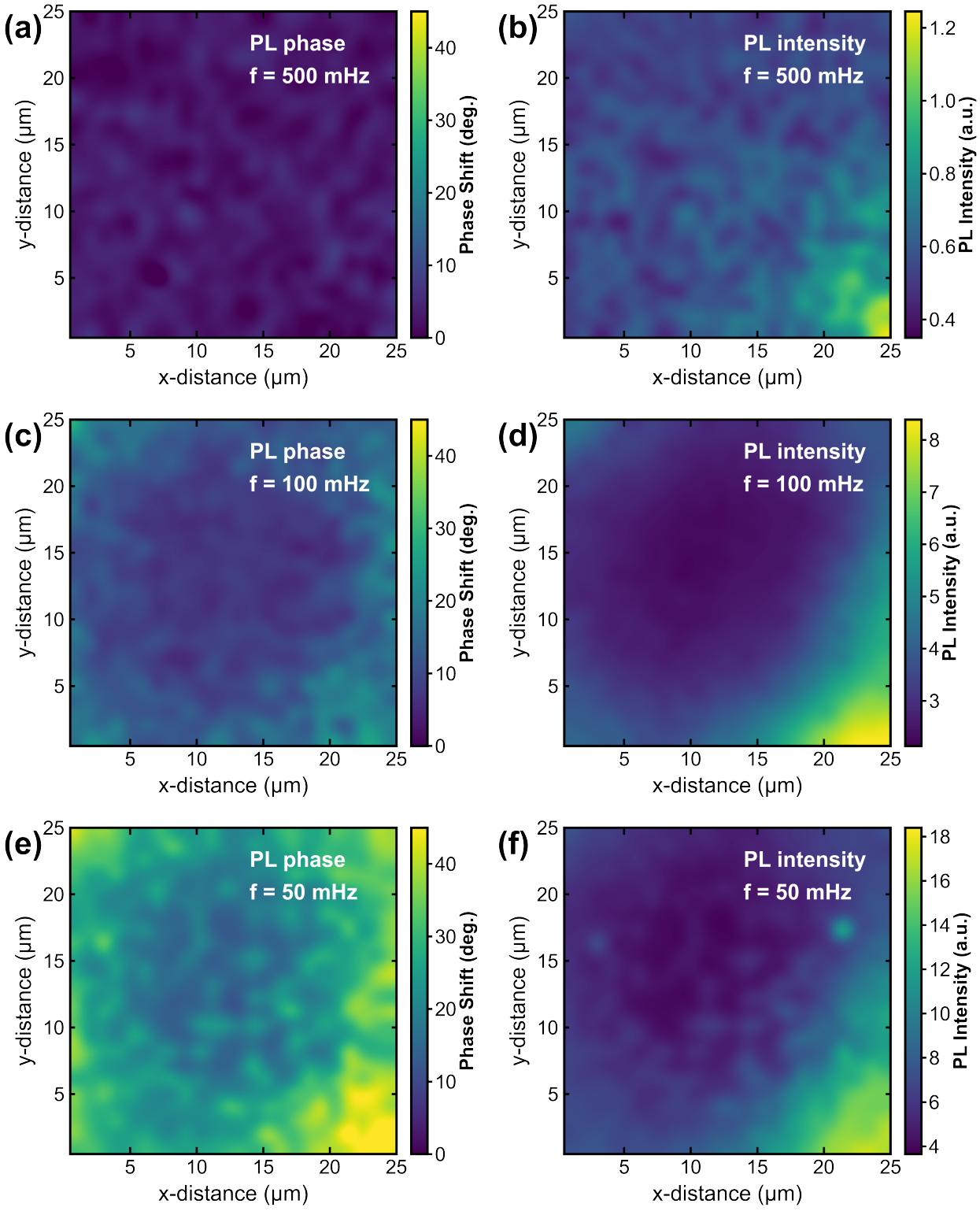

Figure S9: Bicubic-smoothed PL phase shift (left side) and PL intensity (right side) maps over the same sample area at: (a), (b) $f = 500$ mHz; (c), (d) $f = 100$ mHz; (e),(f) $f = 50$mHz.

S4.4 Uncertainty Analysis for IMPLS

To assess the reproducibility in our IMPLS measurements, and to statistically quantify the associated uncertainty arising from both the fitting procedure and sample inhomogeneity, we performed repeated IMPLS measurements at three modulation frequencies (f = 20, 50, 100 mHz) across different points on the sample. For the 100 mHz and 50 mHz cases, $N = 400$ repeated measurements were collected. For the 20 mHz case, a reduced $N = 47$ measurements were collected due to the much longer measurement time required to run the experiment. As mentioned in Section S4.1, the repeated measurements were collected using the home-built pulsed laser microscopy setup, with a focused laser beam spot of 1.7 µm.

Histograms of the PL intensity for each of three selected frequencies are shown in Figures S10a - S10c, where the PL signals are normalized to the average signal across the repeated measurements. In all three cases, the distributions are well described by Gaussian statistics, which are represented by the solid curves over the histograms. As illustrated in Figure S10d, the extracted standard deviations of the fits decrease with increasing frequency. The relative error, defined as RE = $100\% \times \sigma/(\mu\sqrt{N})$ with respect to the mean (μ) was found to be RE = 0.44% for f =100 mHz, RE = 0.82% for f =50 mHz, and RE = 4.33% for f =20 mHz. Linearly extrapolating to the lower frequency limit of f =1 mHz yields a RE of approximately 10%, which we take as the maximum error associated with the PL amplitude (AC) and offset (DC) results. The resulting histograms of the phase shift distributions are shown in Figure S11. As illustrated by the inset, σ similarly decreases with increasing frequency. The relative error ranged between 1.5% and 7% for the three measured frequencies. The offset in the absolute phase values relative to those shown in Figure 3a arises from the different excitation conditions and beam size, since these statistical measurements were collected using the custom-built laser setup. This expanded statistical assessment overall confirms both the reproducibility in the IMPLS results shown in this work, and signifies a relatively low uncertainty associated with each measurement.

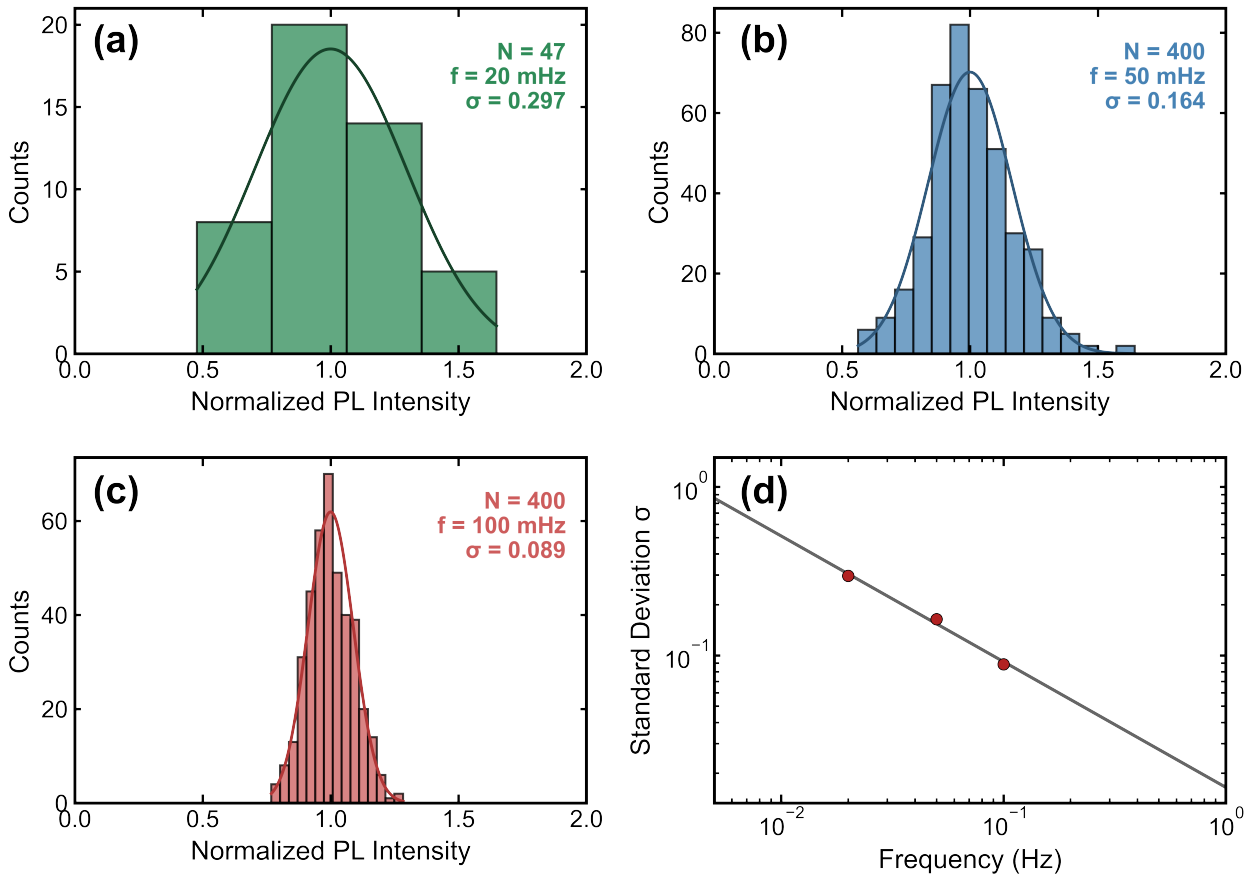

Figure S10: Histograms of the PL intensity distributions measured at (a) $f = 20$ mHz with $N = 47$ measurements, (b) $f = 50$ mHz with $N = 400$ measurements, and (c) $f = 100$ mHz with $N = 400$ measurements. Solid curves indicate Gaussian fits to the data, from which the mean (μ) and standard deviation (σ) were extracted. (d) The frequency dependence of σ determined by the Gaussian fits in panels (a) - (c).

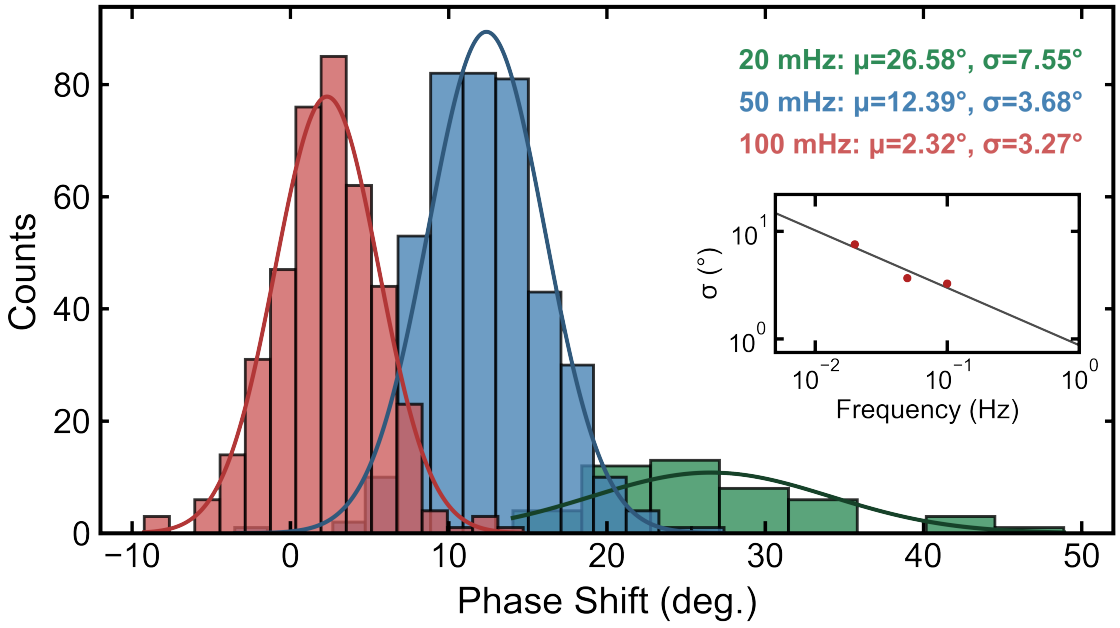

Figure S11: Histograms of the phase shift distributions measured at three modulation frequencies: f = 20 mHz (green), 50 mHz (blue) 100 mHz (red). The inset shows the frequency dependence of σ, with the dark gray line indicating the fit.

S5 IMPLS Phase Shift Correlation with PLQY

As described in the main text, the Δn-dependent phase shift appears similar to the expected PLQY trend as it transitions from low injection levels (LIL) to high injection levels (HIL). To quantify this correlation, we measured the absolute PLQY across the same Δn range and on the same perovskite sample. Localized PLQY maps (25 μm^2) were collected as a function of Δn. In Figure S12a, we overlay the measured PLQY(Δn) with $\theta(\Delta n)$. The scaling between θ (primary y-axis, in red) and PLQY (secondary y-axis, in blue) is arbitrary, but supports the correlation hypothesis.

Using τ_{trap} = 100.5 ns, we fit the experimental PLQY data to[14,15]:

$$\text{PLQY}(\Delta n) = \frac{k_{\text{rad}}\Delta n(\Delta n + p_0)}{\Delta n/\tau_{\text{trap}} + k_{\text{rad}}\Delta n(\Delta n + p_0) + C_{\text{Auger}}\Delta n^2(\Delta n + p_0)} \tag{S4}$$

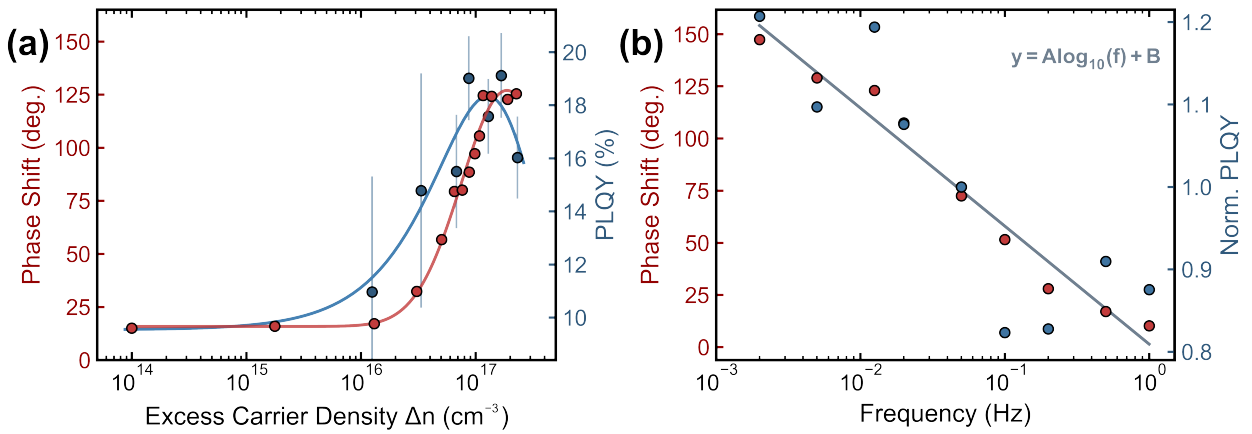

Figure S12: (a) PL phase shift data (red markers) as a function of excess minority carrier density (left axis). Averaged PLQY values (25 measurements per point), with standard deviation error bars are shown with the blue markers (right axis). The blue curve represents the PLQY fit using Equation S4 and red curve represents the phase fit using Equation S5. (b) PL intensity phase shift (red, left axis) and corresponding relative PLQY (blue, right axis) as functions of modulation frequency. Both datasets were fit using $y(f) = A\log_{10}(f) + B$.

With the fit shown by the blue curve in Figure S12a. The radiative and Auger recombination coefficients, and the doping density were then respectively determined as $k_{\text{rad}} = (2.2 \pm 0.97) \times 10^{-11}$ cm^3/s, $C_{\text{Auger}} = (3.2 \pm 2.5) \times 10^{-28}$ cm^6/s and $p_0 = (4.8 \pm 3) \times 10^{16}$ cm^{-3} [15]. While C_{Auger} shows some minor deviation – most likely due to the limited data points collected in the Auger regime – k_{rad} and p_0 are consistent with our previously reported values for a similar perovskite composition[1].

To model the PL phase shift trend across the same Δn range, we applied a simple empirical fit – specifically a logarithmically-scaled Gaussian – to the data. This equation is defined as:

$$\theta(\Delta n) = A \exp\left(\frac{-(\log_{10}(\Delta n) - \mu_{\log})^2}{2\sigma_{\log}^2}\right) + B \tag{S5}$$

where $\mu_{\log}$ and $\sigma_{\log}$ represent the mean and standard deviation in logarithmic space, A is the amplitude and B is the offset. These fit coefficients and their corresponding uncertainties are listed in Table S1. Unlike the physical PLQY model, these coefficients do not represent any physical quantity; this fit is instead used to simply determine at which carrier density does the phase shift reach its peak value as quoted in the main text.

While the peak point differences could reflect different processes separately influencing the phase and PLQY, we postulate that it is more likely a consequence of the different setups used for the two measurements. In particular, the beam diameter of the IMPLS configuration was 6.25 times larger than the beam diameter in the PLQY system. Relating these observations to the frequency-dependent IMPLS response, if we consider θ to be correlated to the PLQY, then the increasing phase shift measured for decreasing frequency (Figure 3a) should also correspond to a rise in the PLQY. We can quantify the frequency-dependent relative PLQY as the PL offset intensity in the frequency-sweep experiment. Overlaying the relative PLQY with the phase shift show that they indeed both exhibit the same logarithmic dependence on f (Figure S12b), meaning a linear correlation to each other.

Table S1: Parameters obtained from fitting $\theta(\Delta n)$ to the logarithmically-scaled Gaussian model (Equation S5). The associated uncertainties of this empirical model were determined directly from nonlinear least-squares analysis.

A (deg.)	B (deg.)	μ (cm^{-3})	$\mu_{\log}$	$\sigma_{\log}$
111.1 ± 4.5	15.81 ± 3.3	$(1.88 \pm 0.16) \times 10^{17}$	17.27 ± 0.04	0.398 ± 0.038

S6 Analytical Model for Lateral Ionic Diffusivity

In this section, we derive and discuss the analytical model applied to estimate the upper limit for the lateral ionic diffusion coefficient (D_{ion}) in the main text. This model is constructed under several assumptions. First, we assume that ionic transport follows a Fickian diffusion model. We simplify the beam geometry and model the laser beam as a cylinder with radius r. Given that AC changes in Δn at the center of the beam are negligible (shown in Figure 5b), we assume that the incident intensity at the center of the beam is constant (DC), while the region where optical modulation becomes dominant is at the beam edge. This defines our diffusion boundary at distance r from the beam center. Calculations to produce Figure 5 are provided in Section S7. Further, given the unchanged phase shift as a function of depth height (Figure S7), we assume that processes in the vertical plane are negligible and we

therefore only model along the lateral plane of the perovskite sample. Finally, we assume that ionic perturbations are small (allowing for linear regime approximation), given the sufficiently small AC excitation perturbation provided by the LED.

With these simplified assumptions in place and justified, we can define two relevant ionic populations: $N(t)$ is the total excess ionic density inside the beam spot, while $N_b(t)$ is the equilibrium ion density at the beam boundary. The rate of change of ions inside the beam spot can be defined using the following rate equation:

$$\frac{dN}{dt} = \frac{N_b(t) - N(t)}{\tau} \tag{S6}$$

Where τ is the ionic exchange time constant. In terms of the geometry of the system, τ is determined by the ratio between the beam volume V, the relevant surface area A, and an effective mass-transfer rate k. Since we only consider lateral effects, the top and rear surface areas are omitted from the total relevant A. Then:

$$\tau = \frac{1}{k}\frac{V}{A} = \frac{1}{k}\frac{\pi r^2 h}{2\pi r h} = \frac{r}{2k} \tag{S7}$$

From Fick's first law of diffusion, the k is related to D_{ion} by the characteristic diffusion length d:

$$k = \frac{D_{\text{ion}}}{d} \tag{S8}$$

In the case where ions are highly diffusive, d is effectively the beam spot radius, $d = r$. Combining Equations S7 and S8 yields:

$$D_{\text{ion}} = \frac{r^2}{2\tau} \tag{S9}$$

Which is effectively reducing the standard expression $D_{\text{ion}} = L^2/2\tau$ to its 1D form[16].

Next, we consider how the ionic population varies in time. Under sinusoidal modulation,

we can write:

$$N_b(t) = N_{b0}e^{i\omega t} \quad \text{and} \quad N(t) = N_0 e^{i\omega t} \tag{S10}$$

Where $\omega = 2\pi f$. Substituting these expressions into Equation S6 yields:

$$N_0 = \frac{N_{b0}}{1 + i\omega t} \tag{S11}$$

Under Fickian diffusion theory, and provided the PL signal is proportional to the net ionic exchange flux (where the flux $J = dN/dt$), combining J with Equation S11 yields:

$$\frac{J}{N_b} = \frac{i\omega t}{1 + i\omega t} \tag{S12}$$

The phase component corresponding to Equation S12 can be written as:

$$\tan(\theta) = \frac{1}{\omega t} \tag{S13}$$

Which, combining with Equation S9 yields:

$$D_{\text{ion}} = \frac{\omega r^2 \tan(\theta)}{2} \tag{S14}$$

At the highly diffusive limit. Since $d \propto r$, this can then be generalized in terms of its characteristic diffusion length which – if known – can be applied to quantify D_{ion}:

$$D_{\text{ion}} = \frac{\omega d^2 \tan(\theta)}{2} \tag{S15}$$

To verify that this analytical model yields consistent and reasonable results, we compare the resulting D_{ion} values obtained when substituting the experimental phase data obtained for $r = 1.7$ µm with the data collected when $r = 3.2$ µm in the main text. The values agree to within 6%, indicating that the model captures the dominant scaling of the response and

that D_{ion} scales with $\omega r^2 \tan(\theta)$.

Though the model captures this general scaling, there are naturally several limitations given its simplicity. First, the model assumes a constant temperature across both the beam spot and the surrounding background. In reality, high-intensity excitation will induce a higher local temperature at the center of the beam compared to the background temperature, which will lead to a higher ionic diffusion coefficient than at room temperature. Moreover, this model poses a limitation in which θ is by definition bound between 0 and 90 degrees. Experimentally, however, both frequency- and Δn-dependent measurements yielded a phase saturation at $\theta \approx 135$ degrees. The additional $\sim$45 degrees phase shift is not accounted for in this model and suggests the presence of additional dynamical processes beyond simple diffusive exchange. Possible origins of this phase shift include ionic formation and recombination pathways, screening effects, multi-step ionic diffusion processes and interfacial processes. Despite these limitations, we model and present how the phase shift evolves for four D_{ion} values ranging between $10^{-8} - 10^{-11}$ cm^2/s. These values were based on previously reported literature values[16–20]. Disregarding the absolute phase shift values, the model reproduces the general trend observed experimentally in this work. Specifically, the model captures the increasing phase shift trend with decreasing frequency (Figure S13a), and the increasing phase shift with decreasing beam radius (Figure S13b). We intend to develop a complete coupled ionic-electronic transport model to capture these additional processes in the near future.

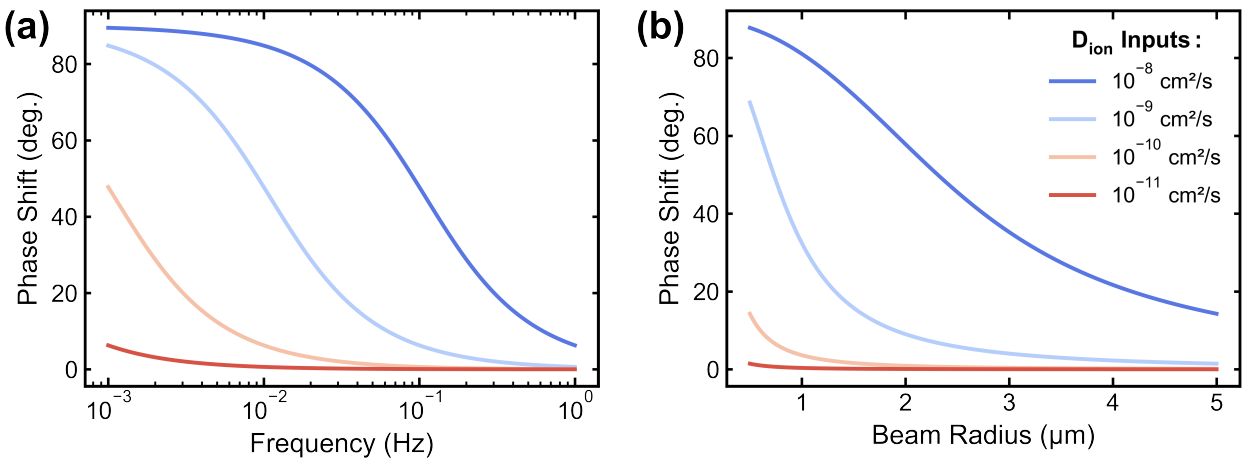

Figure S13: (a) Modeled PL phase shift as a function of frequency at a fixed beam radius $r = 1.7$ µm, and (b) as a function of beam radius at a fixed frequency $f = 50$ mHz. The individual curves represent different D_{ion} values listed in the legend in (b). This model assumes that the characteristic diffusion length is beam radius ($d = r$), and applies Equation S14 to produce the results.

S7 Further Notes on the Diffusion Model

S7.1 Calculations for Constructing the Figure 5

The schematic shown in Figure 5a summarizes relevant material properties across the sample. The schematic was constructed using the beam size and excitation conditions applied in experiment (i) in the main manuscript. The thickness of the perovskite $W_{\text{pvk}} = 560$ nm was determined by profilometry. The absorptance A = 72% was determined from the PLQY measurements, as described in Section S3. The band gap within the laser region ($E_g = 1.584$ eV) and outside of the laser spot ($E_g = 1.608$ eV) was measured by collecting the PL spectra with and without additional laser excitation, and approximating the material band gap at the regions as the PL peak intensity value after converting to the energy scale[21].

In Figure 5b, the intrinsic carrier density n_i was calculated from the band gap. From the band gap, the dark recombination current density at the radiative limit, $J_{0,rad}$ determined

from detailed balance principles, and n_i was solved using[22,23]:

$$n_i = \sqrt{\frac{J_{0,rad}}{q \times W_{pvk} \times k_{rad}}} \tag{S16}$$

In Figure 5c, the Quasi-Fermi Level Splitting (QFLS) was then determined using the standard expression[14]:

$$QFLS = \frac{kT}{q} \ln\left(\frac{np}{n_i^2}\right) \approx \frac{kT}{q} \ln\left(\frac{n[p_0 + n]}{n_i^2}\right) \tag{S17}$$

In Figures 5b and 5c, it is assumed that the charge carriers recombine close to where they were generated. If lateral diffusion of the electronic carriers were included, then the only difference would be a more gradual change in the Δn and QFLS curves, but the general physics remains the same.

S7.2 Alternative Estimation Methods for Ionic Diffusivity

Here, we discuss how our experimental data compares to the literature values for the ionic diffusion coefficient, and propose alternative strategies to estimate the value of the transverse D_{ion} from localized IMPLS data.

To compare with literature, diffusion coefficients for ionic species, such as halide vacancies in mixed halide polycrystalline films, typically range between $D_{\text{ion}} = 10^{-9} - 10^{-11}$ cm^2/s[17–20]. We can relate these coefficients to the diffusion length, L, of the ionic species by[16]:

$$L = \sqrt{D_{\text{ion}}\tau} \tag{S18}$$

In IMPLS, if a mobile ion migrates from the beam center to the region where the modulated excitation becomes relevant ($L \sim r$), the corresponding process time constant is estimated to range between about 4 minutes at 7 hours ($f \approx 6$ µHz - 0.6 mHz). In reality, the mobile ion distribution is not localized to the center of the spot and the averaged time constant will be lower.

In our previous work, we estimated the transverse ionic diffusion coefficient by fitting a complete optical equivalent circuit (OEC) model to the experimental data to extract the characteristic time constant of the process[13]. Here, the DC term is also frequency-dependent; thus from impedance principles, we cannot fit a complete OEC model[24]. However, we can provide an estimation of the relaxation time by fitting the phase data from Figure 3a to the non-ideal Cole-Cole expression:

$$\theta(f) = \theta_0 + \frac{A \sin\left(\frac{\alpha\pi}{2}\right)}{\cosh\left[\alpha \ln\left(\frac{f}{f_{\text{char}}}\right)\right] + \cos\left(\frac{\alpha\pi}{2}\right)} \tag{S19}$$

where f_{char} is the characteristic frequency, α is the non-ideality parameter, and A and θ_0 are amplitude and offset constants[13,25]. The fit (Figure S14) yields $f_{\text{char}} = 3.2 \pm 0.95$ mHz (corresponding to $\tau_{\text{char}} = 49.94 \pm 14.92$ s), and $\alpha = 0.6 \pm 0.1$. The α term is related to diffusivity, where $\alpha = 0.5$ represents a perfect diffusion[24]. Our fit value therefore signifies a diffusive-like process, further supporting our ionic diffusion hypothesis. The low f_{char} explains why we do not observe PL amplitude saturation or the expected turnover in phase as a function of frequency: the associated relaxation frequency is at the limit of the measurement window. Using this value for τ_{char} and $L = r = 5$ µm, the estimated diffusion coefficient from this fit (Equation S18) is $D_{\text{ion}} = 5 \times 10^{-9}$ cm^2/s, falling within the upper limit determined from the analytical model.

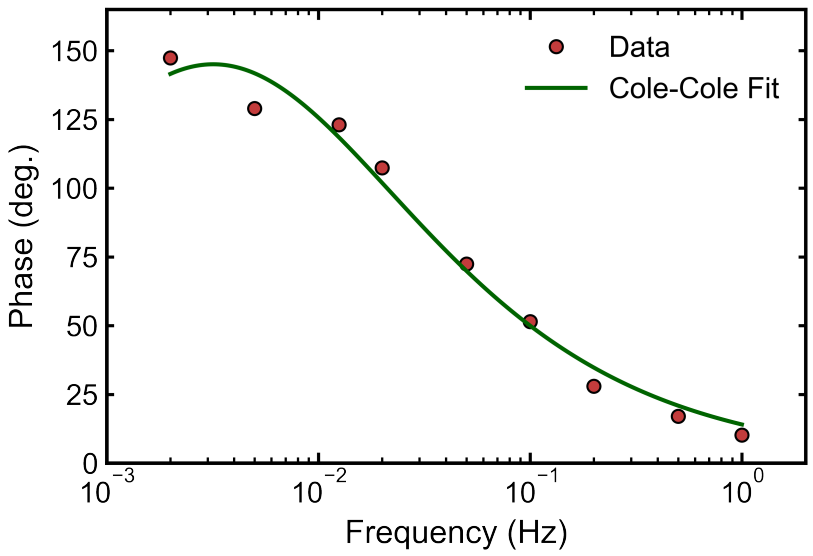

Figure S14: Phase shift data reproduced from Figure 3a of the main text (red), and the Cole-Cole fit to the data using Equation S19 (green).

S8 The Defect Contrast Coefficient

S8.1 Defect Contrast Coefficient Maps

Below we present the collected defect contrast coefficient (DCC, κ) maps as a function of beam size (Figure S15) and as a function of frequency (Figure S16). In the latter case, the maps were collected by repeating measurements over the same sample area (previously shown in Figure S9) and were subsequently bicubic smoothed for visualization.

S8.2 Moran's I Analysis

To quantify whether the observed κ maps exhibit spatial structure beyond random noise, we calculated the global Moran's I statistic for spatial autocorrelation[26]. Moran's I quantifies spatial autocorrelation on a scale from $I = -1$ (perfect dispersion) to $I = 1$ (perfect clustering), with $I = 0$ corresponding to spatial randomness. While Moran's I is widely used in geographical applications, it has recently also been applied to analyze chemical disorder with scanning transmission electron microscopy (STEM) maps[27]. Moran's I for a

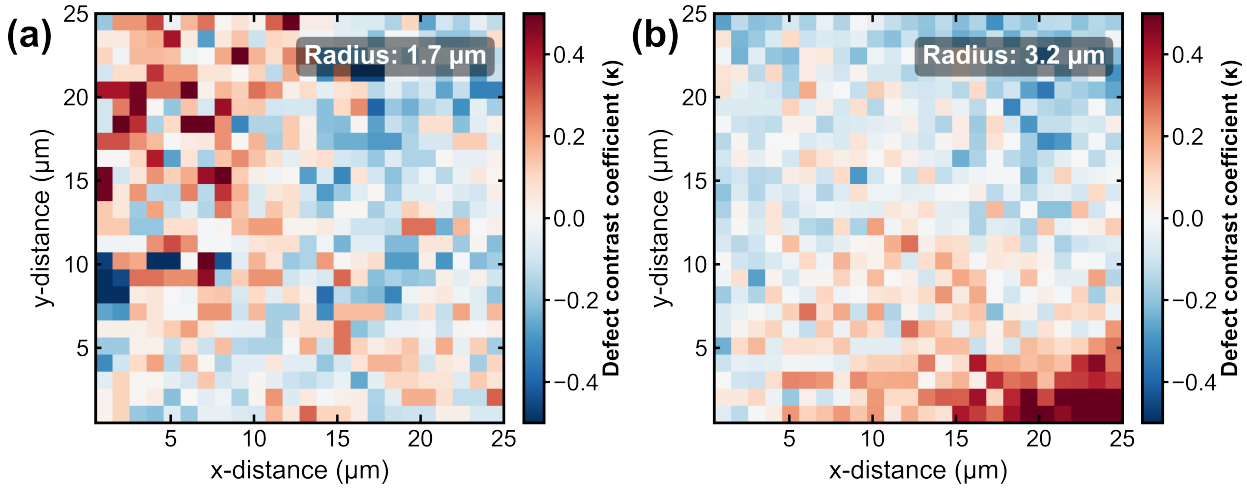

Figure S15: Defect contrast coefficient (κ) maps obtained using Equation 8 from the main text for beam radii of (a) 1.7 µm and (b) 3.2 µm. These maps are the same as those shown in Figure 6 prior to bicubic smoothing.

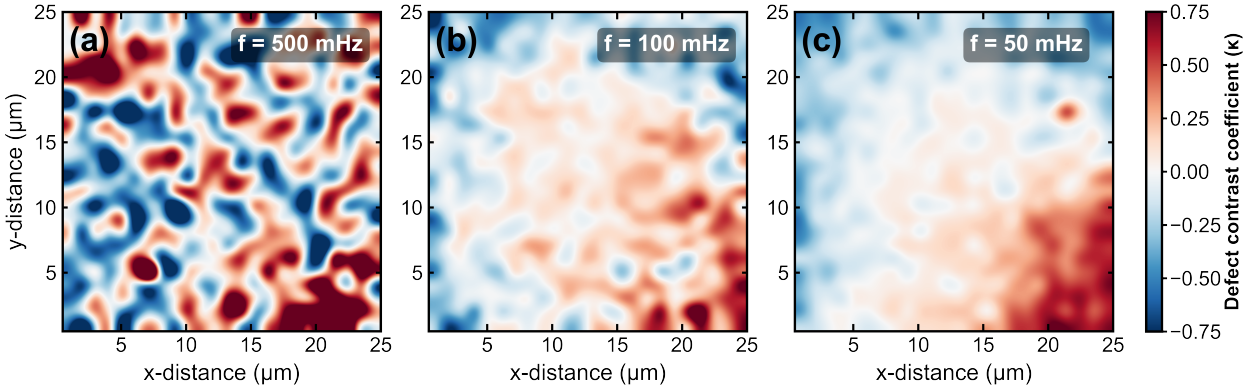

Figure S16: Defect contrast coefficient maps over the same sample area at (a) $f = 500$ mHz, (b) $f = 100$ mHz and (c) $f = 50$ mHz. The maps were constructed from the data shown in Figure S9. κ is scaled to the same range in all three maps as shown with the colorbar.

map containing N pixels is defined as:

$$I = \frac{N}{\sum_i \sum_j w_{ij}} \frac{\sum_i \sum_j w_{ij}(x_i - \bar{x})(x_j - \bar{x})}{\sum_i (x_i - \bar{x})^2}, \tag{S20}$$

where x_i is the value at pixel i, $\bar{x}$ is the mean value over all pixels, and w_{ij} is the spatial weight between pixels i and j. Specifically, w_{ij} determines whether a pair of pixels is considered close enough to contribute to the measure of spatial autocorrelation. Here, we adopted a nearest-neighbor weighting scheme: we set $w_{ij} = 1$ if pixel j is one of the four nearest

neighbors of pixel$i$, and $w_{ij} = 0$ otherwise.

In this work, the κ maps contain $N = 625$ pixels. Statistical significance was assessed using permutation testing with 5,999 random reassignments of pixel values to spatial locations for both κ maps of different beam radii. For the κ maps shown in the main manuscript (Figure S15) the p-values were $< 10^{-4}$, indicating highly significant positive spatial autocorrelation. For the κ maps presented in Figure S16, Moran's I and the p-values are tabulated in Table S2, below. This table importantly signifies that as the frequency increases, Moran's I decreases – signifying an increase in spatial noise. This noise likely corresponds to less mobile defects affecting the PL signal (since at this range, the phase shift is also reduced). Figure S16 with Table S2 serves as a proof of concept that mapping κ as a function of frequency can differentiate species with different mobilities.

Table S2: Moran's I values and the p-values corresponding to the κ maps in Figure S16.

Frequency (mHz)	Moran's I	p-value
500	0.068	2.7×10^{-2}
100	0.224	1.67×10^{-4}
50	0.669	1.67×10^{-4}

References

(1) Gillespie, S. C.; Gautier, J.; van der Burgt, J. S.; Anker, J.; Geerligs, B. L.; Coletti, G.; Garnett, E. C. Silicon-Inspired Analysis of Interfacial Recombination in Perovskite Photovoltaics. *Advanced Energy Materials* **2024**, *14*, 2400965.

(2) Gillespie, S. C.; Thiesbrummel, J.; Gevaerts, V. S.; Geerligs, L. J.; de Boer, J. J.; Coletti, G.; Garnett, E. C. Excitation Intervals Enhance Performance in Perovskite Solar Cells. *ACS Applied Materials & Interfaces* **2025**, *17*, 59476–59485.

(3) Yuan, Y.; Yan, G.; Dreessen, C.; Rudolph, T.; Hülsbeck, M.; Klingebiel, B.; Ye, J.; Rau, U.; Kirchartz, T. Shallow defects and variable photoluminescence decay times up to 280 µs in triple-cation perovskites. *Nature Materials* **2024**, *23*, 391–397.

(4) Krückemeier, L.; Krogmeier, B.; Liu, Z.; Rau, U.; Kirchartz, T. Understanding Transient Photoluminescence in Halide Perovskite Layer Stacks and Solar Cells. *Advanced Energy Materials* **2021**, *11*, 2003489.

(5) Mann, S. A.; Oener, S. Z.; Cavalli, A.; Haverkort, J. E. M.; Bakkers, E. P. A. M.; Garnett, E. C. Quantifying losses and thermodynamic limits in nanophotonic solar cells. *Nature Nanotechnology* **2016**, *11*, 1071–1075.

(6) Knight, A. J.; Wright, A. D.; Patel, J. B.; McMeekin, D. P.; Snaith, H. J.; Johnston, M. B.; Herz, L. M. Electronic Traps and Phase Segregation in Lead Mixed-Halide Perovskite. *ACS Energy Letters* **2019**, *4*, 75–84.

(7) Anaya, M.; Galisteo-López, J. F.; Calvo, M. E.; Espinós, J. P.; Míguez, H. Origin of Light-Induced Photophysical Effects in Organic Metal Halide Perovskites in the Presence of Oxygen. *The Journal of Physical Chemistry Letters* **2018**, *9*, 3891–3896.

(8) Eaton, S. M.; Zhang, H.; Herman, P. R.; Yoshino, F.; Shah, L.; Bovatsek, J.; Arai, A. Y.

Heat accumulation effects in femtosecond laser-written waveguides with variable repetition rate. *Optics Express* **2005**, *13*, 4708–4716.

(9) de Araújo, M. A.; Silva, R.; de Lima, E.; Pereira, D. P.; de Oliveira, P. C. Measurement of Gaussian laser beam radius using the knife-edge technique: improvement on data analysis. *Applied Optics* **2009**, *48*, 393–396.

(10) Motti, S. G.; Meggiolaro, D.; Barker, A. J.; Mosconi, E.; Perini, C. A. R.; Ball, J. M.; Gandini, M.; Kim, M.; De Angelis, F.; Petrozza, A. Controlling competing photochemical reactions stabilizes perovskite solar cells. *Nature Photonics* **2019**, *13*, 532–539.

(11) Herz, L. M. Charge-Carrier Mobilities in Metal Halide Perovskites: Fundamental Mechanisms and Limits. *ACS Energy Letters* **2017**, *2*, 1539–1548.

(12) Lim, J.; Kober-Czerny, M.; Lin, Y.-H.; Ball, J. M.; Sakai, N.; Duijnstee, E. A.; Hong, M. J.; Labram, J. G.; Wenger, B.; Snaith, H. J. Long-range charge carrier mobility in metal halide perovskite thin-films and single crystals via transient photoconductivity. *Nature Communications* **2022**, *13*, 4201.

(13) Gillespie, S. C.; Alvarez, A. O.; Thiesbrummel, J.; Gevaerts, V. S.; Geerligs, L.; Ehrler, B.; Coletti, G.; Garnett, E. C. Intensity-Modulated Photoluminescence Spectroscopy for Revealing Ionic Processes in Halide Perovskites. *ACS Energy Letters* **2025**, *10*, 3122–3131.

(14) Ross, R. T. Some Thermodynamics of Photochemical Systems. *The Journal of Chemical Physics* **1967**, *46*, 4590–4593.

(15) Kirchartz, T.; Márquez, J. A.; Stolterfoht, M.; Unold, T. Photoluminescence-Based Characterization of Halide Perovskites for Photovoltaics. *Advanced Energy Materials* **2020**, *10*, 1904134.

(16) Peng, W.; Aranda, C.; Bakr, O. M.; Garcia-Belmonte, G.; Bisquert, J.; Guerrero, A. Quantification of Ionic Diffusion in Lead Halide Perovskite Single Crystals. *ACS Energy Letters* **2018**, *3*, 1477–1481.

(17) Futscher, M. H.; Lee, J. M.; McGovern, L.; Muscarella, L. A.; Wang, T.; Haider, M. I.; Fakharuddin, A.; Schmidt-Mende, L.; Ehrler, B. Quantification of ion migration in $CH_3NH_3PbI_3$ perovskite solar cells by transient capacitance measurements. *Materials Horizons* **2019**, *6*, 1497–1503.

(18) McGovern, L.; Futscher, M. H.; Muscarella, L. A.; Ehrler, B. Understanding the Stability of $MAPbBr_3$ versus $MAPbI_3$: Suppression of Methylammonium Migration and Reduction of Halide Migration. *The Journal of Physical Chemistry Letters* **2020**, *11*, 7127–7132.

(19) McGovern, L.; Grimaldi, G.; Futscher, M. H.; Hutter, E. M.; Muscarella, L. A.; Schmidt, M. C.; Ehrler, B. Reduced Barrier for Ion Migration in Mixed-Halide Perovskites. *ACS Applied Energy Materials* **2021**, *4*, 13431–13437.

(20) Schmidt, M. C.; Alvarez, A. O.; de Boer, J. J.; van de Ven, L. J.; Ehrler, B. Consistent Interpretation of Time- and Frequency-Domain Traces of Ion Migration in Perovskite Semiconductors. *ACS Energy Letters* **2024**, *9*, 5850–5858.

(21) Mooney, J.; Kambhampati, P. Get the Basics Right: Jacobian Conversion of Wavelength and Energy Scales for Quantitative Analysis of Emission Spectra. *The Journal of Physical Chemistry Letters* **2013**, *4*, 3316–3318.

(22) Shockley, W.; Queisser, H. J. Detailed Balance Limit of Efficiency of p-n Junction Solar Cells. *Journal of Applied Physics* **1961**, *32*, 510–519.

(23) Wolff, C. M.; Bourelle, S. A.; Phuong, L. Q.; Kurpiers, J.; Feldmann, S.; Caprioglio, P.; Marquez, J. A.; Wolansky, J.; Unold, T.; Stolterfoht, M.; Shoaee, S.; Deschler, F.;

Neher, D. Orders of Recombination in Complete Perovskite Solar Cells – Linking Time-Resolved and Steady-State Measurements. *Advanced Energy Materials* **2021**, *11*, 2101823.

(24) Lazanas, A. C.; Prodromidis, M. I. Electrochemical Impedance Spectroscopy - A Tutorial. *ACS Measurement Science Au* **2023**, *3*, 162–193.

(25) Cole, K. S.; Cole, R. H. Dispersion and Absorption in Dielectrics I. Alternating Current Characteristics. *The Journal of Chemical Physics* **1941**, *9*, 341–351.

(26) Moran, P. A. P. Notes on Continuous Stochastic Phenomena. *Biometrika* **1950**, *37*, 17–23.

(27) Xu, M.; Kumar, A.; LeBeau, J. M. Correlating local chemical and structural order using Geographic Information Systems-based spatial statistics. *Ultramicroscopy* **2023**, *243*, 113642.